Article

Cholesterol-Enriched Domain Formation Induced by Viral-Encoded, Membrane-Active Amphipathic Peptide

Joshua M. Hanson,[1] Douglas L. Gettel,[2] Seyed R. Tabaei,[3,4] Joshua Jackman,[3,4] Min Chul Kim,[3,4] Darryl Y. Sasaki,[5] Jay T. Groves,[6,7] Bo Liedberg,[3,4] Nam-Joon Cho,[3,4,8] and Atul N. Parikh[1,2,3,4,9,*]

[1]Biophysics Graduate Group and [2]Department of Chemical Engineering & Materials Science, University of California, Davis, Davis, California; [3]Centre for Biomimetic Sensor Science and [4]School of Materials Science and Engineering, Nanyang Technological University, Singapore; [5]Biotechnology and Bioengineering Department, Sandia National Laboratories, Livermore, California; [6]Chemistry Department, University of California, Berkeley, California; [7]Mechanobiology Institute, National University of Singapore, Singapore; [8]School of Chemical and Biomedical Engineering, Nanyang Technological University, Singapore; and [9]Department of Biomedical Engineering, University of California, Davis, Davis, California

ABSTRACT The α-helical (AH) domain of the hepatitis C virus nonstructural protein NS5A, anchored at the cytoplasmic leaflet of the endoplasmic reticulum, plays a role in viral replication. However, the peptides derived from this domain also exhibit remarkably broad-spectrum virocidal activity, raising questions about their modes of membrane association. Here, using giant lipid vesicles, we show that the AH peptide discriminates between membrane compositions. In cholesterol-containing membranes, peptide binding induces microdomain formation. By contrast, cholesterol-depleted membranes undergo global softening at elevated peptide concentrations. Furthermore, in mixed populations, the presence of ~100 nm vesicles of viral dimensions suppresses these peptide-induced perturbations in giant unilamellar vesicles, suggesting size-dependent membrane association. These synergistic composition- and size-dependent interactions explain, in part, how the AH domain might on the one hand segregate molecules needed for viral assembly and on the other hand furnish peptides that exhibit broad-spectrum virocidal activity.

INTRODUCTION

The rapid rise in the number of emerging and reemerging infectious diseases due to viral pathogens underscores the need for therapeutic approaches that can target large classes of viruses using single drugs (1). To be effective, such one-for-many broad-spectrum antivirals must either 1) interfere with the shared steps of biophysical or biochemical processes of viral entry (i.e., fusion-inhibiting mechanisms) (2,3), or 2) disable disparate virions by targeting their common structural components (i.e., virocidal mechanisms). To this end, one obvious target is the lipid bilayer component of the viral envelope. Although it is derived from the host cell, the viral membrane differs from cellular membranes in many physical-chemical properties, including chemical composition, curvature, and lateral fluidity, as well as the absence of a biogenic reparative capacity. These attributes are shared across a variety of different viruses, rendering the viral membrane a discrete and susceptible target for developing broad-spectrum antivirals. Specifically, antiviral drug candidates can be designed to selectively alter the nanometer-scale viral envelope (without harming the larger host cell membrane), thereby destabilizing its structural integrity and/or disrupting the ability of the virus to enter the host cell. Indeed, a number of different membrane-active molecules, such as lysophosphocholines (4), the so-called rigid amphipathic fusion inhibitors (5), and thiazolidine-based lipophilic compounds (e.g., LJ001 (6)), show potential as broad-spectrum antivirals. The membrane activity of these molecules involves binding, insertion, or oxidative alteration of the viral membranes, all of which act to stabilize fusion-inhibiting positive viral-membrane curvatures, impeding the transition from positive-to-negative curvatures that is necessary for successful virus-cell fusion (3).

In this same vein, peptides derived from viral proteins are potentially attractive membrane-targeting candidates for viral inhibition. It is now well accepted that the translation (and posttranslational modification) of the viral genome produces gene products whose functional domains often provide inhibitory activity, which typically is limited to the source virus (7–9). A notable case is the class of amphipathic α-helical (AH) peptides (Fig. S1 in the Supporting Material) (10). These peptides are derived from the highly conserved, N-terminal membrane anchor domain of the hepatitis C virus (HCV) nonstructural protein NS5A (11), which shows strikingly broad-spectrum inhibitory activity (see below).

As a viral gene product with inhibitory activity, the class of AH peptides is unique with respect to both its origin and mechanism of antiviral action. First, the large variety of

Submitted August 18, 2015, and accepted for publication November 17, 2015.

*Correspondence: anparikh@ucdavis.edu

Joshua M. Hanson and Douglas L. Gettel contributed equally to this work.

Editor: Tobias Baumgart.

0006-3495/16/01/0176/12

http://dx.doi.org/10.1016/j.bpj.2015.11.032

existing antiviral peptides, derived from structural proteins in the viral envelope, act by blocking fusion and entry by mimicking viral ligand-host receptor interactions or by inhibiting fusion protein activity at the virus-cell interface (12). By contrast, neither the NS5A protein nor its AH fragment is packaged in the mature virion. Rather, NS5A, a 56 kDa homodimeric RNA-binding phosphoprotein produced by proteolytic processing of the single ~3000-amino-acid polyprotein encoded by the 9.6-kb single-stranded HCV RNA (13), binds to the endoplasmic reticulum (ER) membranes of the host cell. Specifically, the AH moiety binds, purportedly via phosphoinositide receptors (14), to the cytosolic leaflet in a membrane-parallel (in-plane) manner, locally modifying the ER membrane (11). This genetically encoded membrane-binding property also confers to the AH moiety an unexpected lytic behavior against virion membranes (15). Indeed, recent studies suggested that the AH peptide inhibits virus infectivity by direct virocidal activity, rather than by inhibiting viral entry (10,15). These studies showed that peptide association compromises the structural integrity of the virus through membrane lysis. This in turn frees the viral capsid, exposing the viral genome to exonucleases and ultimately leading to degradation of the virus. Although some studies have advanced geometric arguments invoking the size and curvature dependence of the interactions between the AH peptide and the viral membrane envelope (14,15), the molecular mechanisms by which AH peptides discriminate among and disrupt viral membranes to achieve broad-spectrum virocidal activity against cholesterol (Ch)-laden, raft-forming virions are largely unknown (see below).

Second, and perhaps more important in terms of therapeutics, the antiviral activity of the AH peptide is not limited to the virus of origin, i.e., HCV. These peptides exhibit potent, broad-spectrum antiviral activity against several disparate viruses, including the West Nile and dengue viruses of the *Flaviviridae* family, paramyxoviruses (e.g., measles and respiratory syncytial virus), and HIV (10). This extended antiviral activity spectrum stems from the ability of AH peptides to target shared lipid components of viral envelopes rather than virus-encoded proteins (10,16). Interestingly, membranes of viruses inhibited by the AH peptide share a common lipid composition, which includes lipid raft-forming mixtures containing Ch and sphingomyelin (SM) (17). Specifically, HCV, West Nile virus, and dengue virus, which bud into the ER, naturally share a raft-enriched lipid composition such as that sequestered by the membrane anchor domain of NS5A, which drives replication (18). Similarly, although the paramyxoviruses (i.e., measles and respiratory syncytial virus) (19,20) and HIV (21) emerge from the plasma membrane, they also accumulate raft-partitioning components, presumably by selecting cell-surface locations containing raft microdomains for budding during viral maturation (22). Based on this consideration, it seems likely that the specificity of AH peptides for the viral membrane might arise from their ability to recognize viral membrane compositions (10); however, this remains to be verified.

From a biophysical point of view, it is notable that the AH-mediated association of NS5A with the ER membrane plays critical roles in the viral life cycle (23). One important function of NS5A, in conjunction with other nonstructural proteins, is to induce dramatic remodeling of the ER membrane, producing double- and multimembrane vesicles (DMVs and MMVs, respectively) (24,25). These vesicles become part of the so-called membranous web, a collection of highly heterogeneous vesicles held together by an amorphous matrix (24,26). This web serves as a platform for viral RNA replication by locally increasing the concentrations of viral factors and host-cell components that drive viral replication (11,16,27). However, the mechanisms by which such large-scale remodeling of the ER membrane, including molecular rearrangements to localize specialized lipids, and the topological transitions needed to create DMVs and MMVs, remain incompletely understood (25). We reasoned that the AH-mimetic peptide could also serve as a probe of NS5A-membrane interactions, further elucidating its contributions to the formation of the membranous web.

In the work reported here, we probe the membrane interactions of a potent AH-mimetic peptide using protein- and cytosol-free model phospholipid membranes of closed topologies, i.e., giant unilamellar vesicles (GUVs). We find that interactions with the synthetic AH peptide induce distinctly different structural perturbations in model membranes depending on their chemical composition. Model membrane compositions incorporating raft-forming lipid mixtures containing SM and Ch exhibit a striking redistribution of membrane molecules upon peptide binding, producing optically resolved domains. The fluid and compositionally uniform membranes devoid of phase-separating membrane components, by contrast, reveal little or no perturbations at comparable peptide concentrations. At substantially higher peptide concentrations, these uniform membranes soften, producing global, vigorous fluctuations or flickering of the membrane boundary upon interaction with the AH peptide. In either case, the peptide association does not permanently disrupt the closed topologies of vesicular membranes, but transiently permeabilizes the membrane, allowing for transmembrane solute transport. Furthermore, competition assays employing coexisting populations of large unilamellar vesicles (LUVs) and GUVs reveal that for either composition, the presence of LUVs suppresses peptide-induced physical perturbations in GUVs and also traffics lipids to the membrane surface of GUVs in a composition-dependent manner. Taken together, these results reveal that the interactions of the AH peptide-probe with topologically closed lipid bilayers depend on the chemical composition and rearrange the membrane molecular distributions, suggesting in part how NS5A might alter the ER membrane to allow formation of

the membranous web, and how the class of AH peptides might derive their broad-spectrum antiviral properties against Ch-laden viral particles.

MATERIALS AND METHODS

Materials

1-Palmitoyl-2-oleoyl-*sn*-glycero-3-phosphocholine (POPC), egg SM, Ch, and lissamine rhodamine B 1,2-dioleyl-*sn*-glycero-3-phosphoethanolamine (Rho-B DOPE) were acquired from Avanti Polar Lipids (Alabaster, AL). Glucose was obtained from Sigma-Aldrich (St. Louis, MO), and 2-deoxy-2-[(7-nitro-2,1,3-benzoxadiazol-4-yl) amino]-D-glucose (2-NBDG) was obtained from Cayman Chemical (Ann Arbor, MI). Sucrose was obtained from EMD Chemicals (Philadelphia, PA). Chloroform, sodium chloride (NaCl), dimethyl sulfoxide (DMSO), and Avidin, NeutrAvidin, Oregon Green 488 conjugate were purchased from Thermo Fisher Scientific (Waltham, MA). Texas Red 1,2-dihexadecanoyl-*sn*-glycero-3-phosphoethanolamine, triethylammonium salt (Texas Red DHPE) and head-labeled N-(7-nitrobenz-2-oxa-1,3-diazol-4-yl)-1,2-dihexadecanoyl-*sn*-glycero-3-phosphoethanolamine, triethylammonium salt (NBD-PE) were purchased from Life Technologies (Carlsbad, CA). Dulbecco's phosphate-buffered saline 1X (DPBS) without calcium chloride and magnesium chloride was purchased from Gibco (Grand Island, NY). Tris-HCl (1 M solution, pH 7.0) was purchased from Affymetrix (Santa Clara, CA). AH peptide (>95%) and AH peptide labeled with 5-carboxytetramethylrhodamine (5-TAMRA) (N-term→C-term 5-TAMRA-SGSWLRDVWDWICTVLT DFKTWLQSKL-OH, pI 6.81) were acquired from Anaspec (Fremont, CA). The procedure used to synthesize DP-EG10-biotin is described elsewhere (28). All chemicals were used without further purification.

Glass-bottom, 96-well plates were obtained from MatTek (Ashland, MA). Indium tin oxide (ITO)-coated glass slides (resistance 5–25 Ω) were obtained from Delta Technologies (Loveland, CO). Manual Teflon-tipped syringes were purchased from Agilent Technologies (Santa Clara, CA).

Preparation of model membranes

GUVs

GUVs were prepared by electroformation according to a published protocol (29,30). Briefly, we began by preparing stock solutions consisting of the desired molar composition of lipid components in chloroform at 1–2 mg/mL. Model membranes of single-component GUVs were composed of POPC. Raft-forming viral envelope mimetic compositions were modeled with equimolar mixtures of POPC, egg-SM, and Ch. In both cases, experiments were performed by doping the GUVs with trace concentrations of single labeled lipids, which included Rho-B DOPE (1%), Texas Red DHPE (1%), or NBD-PE (1–3%). To fluorescently label both liquid-disordered (L_d) and liquid-ordered (L_o) phases in raft mixtures, we performed selected experiments by doping the L_o phase with DP-EG10-biotin (3%), which binds to labeled NeutrAvidin, and the L_d phase with Rho-B DOPE (1%). In these experiments, the molar ratios for POPC/egg-SM/Ch/DP-EG10-biotin/Rho-B DOPE were 32:32:32:3:1. In all cases, small droplets (15–30 μL) of stock solution were spread on the conductive side of each of two ITO-coated slides (5–25 Ω) as the chloroform evaporated. The slides were then further dried in a vacuum desiccator for at least 1 h. A chamber was formed by sandwiching a 1-mm-thick rubber O ring (Ace Hardware, Davis, CA) sealed with high-vacuum grease (Dow Corning, Midland, MI) between the conductive sides of the two ITO-coated slides. After the ring was attached to one of the slides, the dried film was hydrated with either 50 mM or 300 mM sucrose solution in deionized water. The second ITO-coated slide was placed over the ring, sealing the chamber and ensuring that no visible air bubbles were trapped inside. Using a function generator, a 4.0 V(pp) AC sine wave was applied across the two slides at 10 Hz for 1–2 h, followed by a 4.0 V(pp) square wave at 2 Hz for 1–2 h. During the formation of GUVs, the chamber was covered to protect from light. After GUV formation was observed, the ITO formation chamber was disassembled and the solution containing GUVs was pipetted off and used immediately or stored in small centrifuge tubes at 4°C. Vesicles were used within a week of preparation.

Preparation of LUVs

LUVs were prepared according to a previously described vesicle extrusion method (31). Stock solutions of lipids in chloroform (POPC or raft-forming ternary mixtures consisting of POPC, Ch, and SM) were prepared in glass vials at 1–2 mg/mL in equimolar proportions. In both cases, 1 mol % Rho-B DOPE was added to enable fluorescence visualization. The chloroform was evaporated under nitrogen and subsequently dried under vacuum for at least 1 h. The dried lipid was then rehydrated in 300 mM sucrose at 1–2 mg/mL for use in competition assay experiments. Rehydrated lipids were sonicated for several minutes and gently inverted before extrusion. The solutions were subsequently passed through a Mini-Extruder (Avanti Polar Lipids) 21 times at room temperature for POPC and at 50°C for raft-forming mixtures. The extruder was assembled with a 100 nm polycarbonate membrane and two 1 mL gas-tight syringes from Hamilton (Reno, NV). The vesicles were then utilized in competition assay experiments the same day they were extruded.

Peptide incubation assays

Preparation of AH peptide stock solution

AH peptide and 5-TAMRA-AH peptide at a stock concentration of 2.6 mM (10 mg/mL in 180 mM NaCl, 9 mM Tris-HCl pH 7, 10% DMSO by volume) were divided into 20 μL aliquots and stored in a freezer at −20°C. In preparation for incubation experiments, the aliquots were each diluted with 180 μL of 333 mM glucose in deionized water to make a solution of 260 μM AH peptide in 18 mM NaCl, 0.9 mM Tris-HCl, 300 mM glucose, 1% DMSO by volume. Once the stock aliquots were thawed and diluted, they were stored in a refrigerator at 4°C.

GUV incubation with AH peptide and 5-TAMRA-AH peptide

Glass-bottom, 96-well plates (MatTek) were used for all tests utilizing a spinning-disk confocal fluorescence microscope. A typical incubation experiment had 180–200 μL total volume per well. First, GUVs were prepared as described above in either 50 mM or 300 mM sucrose. Based on the formation yield, an aliquot of GUV stock solution from 1–5 μL was added to a well with a large excess of isotonic glucose solution to osmotically balance and sediment the vesicles to the bottom. Control experiments were performed without the addition of AH peptide. Vesicles were then incubated with 0.5–35 μM AH peptide (prepared as described above), which was added slowly by micropipette injection over 15–20 s, leaving the vesicles mostly unperturbed. Labeled peptide solutions consisted of either a 100% 5-TAMRA-AH peptide solution (POPC GUV) or a mixture of 50% 5-TAMRA-AH and 50% unlabeled AH peptide (POPC raft GUV). Additional details regarding the incubation experiments are described below. All observations were performed at room temperature.

Fluorescence visualization of GUV L_o and L_d phase separation induced by AH peptide

GUVs consisting of POPC/egg-SM/Ch/DP-EG10-biotin/Rho-B DOPE (32:32:32:3:1) were prepared in 300 mM sucrose and balanced with a mixture of 300 mM glucose (93%) and 1× PBS pH 7.2 (7%) in the exterior before incubation experiments were conducted. The vesicles were then incubated with 2 μM AH peptide. The L_o probe DP-EG10-biotin (synthesized as described previously (28)) was visualized by binding to NeutrAvidin Oregon Green 488 (1 μM incubation). The binding was

immediate and strong, and no washing steps were required to achieve easily discernible bright membrane fluorescence.

Membrane leakage assay

GUVs were prepared as described above, with mixtures consisting of POPC/Rho-B DOPE (99:1) and POPC/egg-SM/Ch/Rho-B DOPE (33:33:33:1). Vesicles were formed with 300 mM sucrose inside and balanced with 300 mM glucose outside before incubation experiments were conducted. Before the POPC vesicles were incubated with 10 μM AH peptide, 2-NBDG (stock 2.9 mM in Milli-Q water) was added to the vesicle exterior (28 μM). Before the raft mixture was incubated with 4 μM AH peptide, 2-NBDG (stock 2.9 mM in Milli-Q water) was added to the vesicle exterior (40 μM). Red and green channels were simultaneously monitored to observe any peptide-induced leakage of the 2-NBDG across GUV membranes into the vesicle interior. Leakage was quantified by comparing interior and exterior fluorescence intensities over time.

Competition assay: simultaneous incubation of GUVs and LUVs with AH peptide

GUVs and LUVs consisting of POPC/Rho-B DOPE (99:1) and POPC/NBD-PE (99:1), respectively, were prepared in 300 mM sucrose as described above. For AH peptide incubation experiments, a total volume of ~180–200 μL was used. GUVs were added first, followed by LUVs. The typical concentrations of LUVs and GUVs were 1.3–3.0 μg/mL and 1.3–1.4 μg/mL, respectively. Before incubation with AH peptide, green (NBD-PE, GUVs) and red (Rho-B DOPE, LUVs) fluorescence was analyzed to confirm the absence of unmediated interactions between GUVs and LUVs. After incubation with AH, fluorescence was imaged in both red and green channels. The resulting images were analyzed for both colocalization of fluorescent probes and recovery after photobleaching (see below).

Characterization

Fluorescence microscopy

Spinning-disk confocal microscopy measurements were carried out on an Intelligent Imaging Innovations Marianas Digital Microscopy Workstation (3i, Denver, CO) fitted with a CSU-X1 spinning-disk head (Yokogawa; Musashino-shi, Tokyo, Japan) and a Quantem512SC EMCCD camera (Photometrics, Tucson, AZ). For measurements, we used oil immersion objectives (Zeiss Fluor 40x (NA 1.3), Zeiss Plan-Fluor 63x (NA 1.4), and Zeiss Fluor 100x (NA 1.46); all from Carl Zeiss, Oberkochen, Germany). Rho-B DOPE (Ex/Em 560:583), TR-DHPE (Ex/Em 595/615), and 5-TAMRA (Ex/Em 541:568) were exposed with a 50 mW 561 laser line, and NBD-PE (Ex/Em 463:536), NeutrAvidin Oregon Green 488 (Ex/Em 496:524), and 2-NBDG (Ex/Em 465:540) were exposed with a 50 mW 488 laser line. Time-lapse images were acquired at one to three frames per second. The images were subsequently processed using ImageJ (a public-domain software; http://rsbweb.nih.gov/ij/) and Slidebook digital microscopy imaging software (3i).

Fluorescence recovery after photobleaching experiments for GUV-LUV competition assays

Fluorescence recovery after photobleaching (FRAP) experiments were performed with a 50 mW 561 laser line or a 50 mW 488 laser line (32). Vesicles were viewed in the equatorial plane with a 63x objective and a Quantem512SC EMCCD camera, giving a 512 $\times$ 512 pixel image. Rho-B DOPE and NBD-PE fluorescent probes were bleached in a rectangular region along the contour of the GUV (10–12 μm long) at 60% of maximum laser power. Recovery of fluorescence was recorded and measured from the subsequent 60–300 frames at one to two frames per second. The fluorescence recovery of each vesicle was fit to the following equation:

$$\mathrm{F(t)} = \left(\mathrm{F}_{rec} - \mathrm{F}_{post}\right)\left(1 - e^{-\frac{t}{\tau}}\right) + \mathrm{F}_{post}.$$

The fitting enabled us to estimate the half-time for recovery, $\tau_{1/2} = \tau \log(2)$, where F_{rec} is the fluorescence after recovery and F_{post} is the fluorescence immediately after bleaching. The diffusion coefficient was calculated as $D = (r_e^2 + r_n^2)/8\tau_{1/2}$, where r_n is the radius of the user-defined bleached spot and r_e is the effective radius calculated from the postbleach profile (33).

Calculation of bending moduli, K_c, from GUV fluctuation analysis

Each vesicle contour was determined from a two-dimensional cross section for each time point. The vesicle edge was calculated using a previously developed MATLAB (The MathWorks, Natick, MA) code (34). In short, based on a user-defined center of mass and approximate radius, the image was sliced into angular wedges. For each slice, the edge was located using the maximum radial intensity gradient and a local parabolic fit. The bending moduli and membrane tension were then estimated from subsequent calculations based on the determined edge profiles (above) as described previously (34–36).

RESULTS AND DISCUSSION

Binding-induced domain formation in viral-membrane-mimicking GUVs

We begin by investigating viral-membrane-mimicking (18) model GUVs (15–30 μm diameter) (30) consisting of ternary lipid mixtures composed of an unsaturated phospholipid, POPC, Ch, and egg-SM in equimolar proportions (see Materials and Methods). Depending on the composition and temperature, these mixtures are known to form a uniform single phase or exhibit phase separation (37). The latter is characterized by two coexisting liquid phases: a dense phase enriched in SM and Ch (designated the L_o phase) and a second, less dense phase consisting primarily of POPC (the L_d phase). To discriminate between the L_o and L_d phases by fluorescence microscopy, we doped the GUVs with a small concentration (1 mol %) of a phase-sensitive probe, Rho-DOPE (Ex/Em 560:583 nm) (38). At the equimolar (1:1:1) composition, the phase diagram predicts the absence of domain formation at optical length scales (37), but does not rule out the existence of nanoscale domains (39). Consistent with this prediction, the GUVs encapsulating 300 mM sucrose appear optically homogeneous at room temperature in an osmotically balanced, isotonic medium containing 300 mM glucose (Fig. 1, *ai* and *ei*).

Administering AH peptide (1–5 μM) to a population of GUVs prompts a striking change in the membrane molecular organization, as revealed by the gross redistribution of the phase-sensitive fluorophore (i.e., Rho-DOPE). The initially homogeneous fluorescence is quickly lost, replaced by an inhomogeneous one characterized by the presence of randomly distributed, fluorophore-enriched circular domains (Fig. 1, *a* and *b*; Movies S1 and S2). Because Rho-DOPE partitions preferentially into the L_d phase (38), the

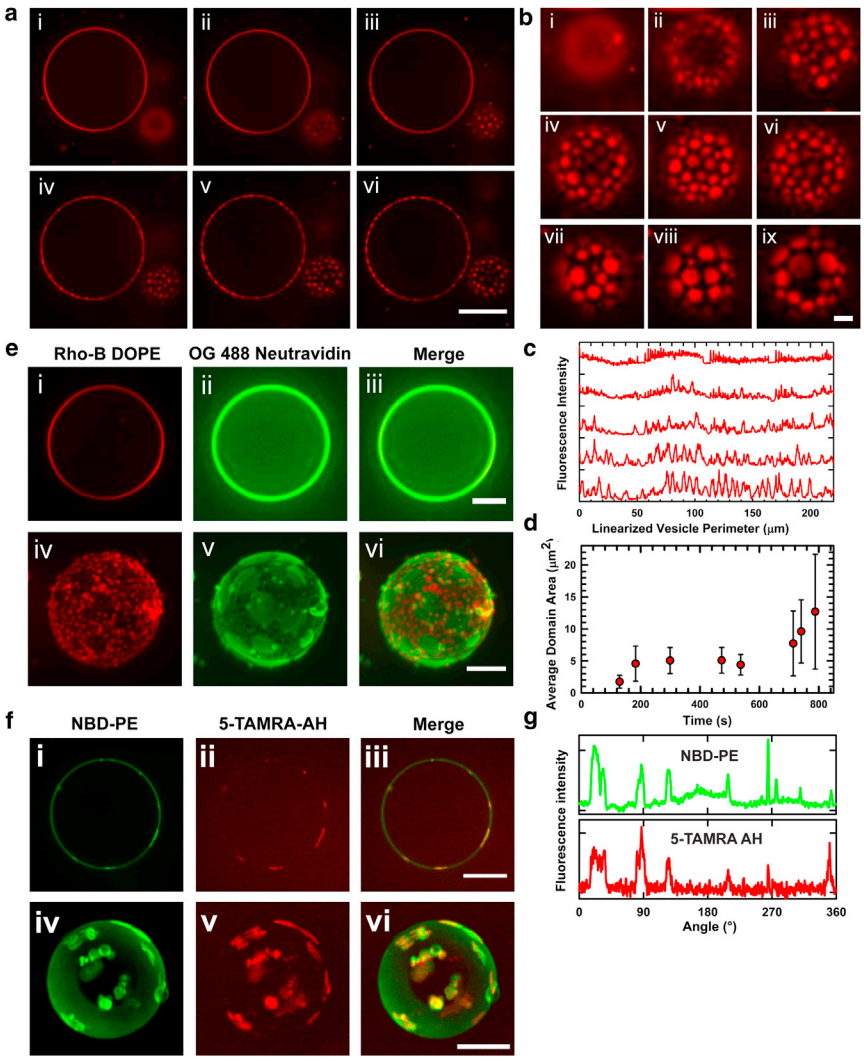

FIGURE 1 AH-peptide-induced lateral reorganization in raft-forming GUVs. (*a* and *b*) Fluorescence images of raft-forming GUVs consisting of equimolar concentrations of POPC, SM, and Ch doped with Rho-B DOPE upon incubation with 5 μM AH peptide. (*a*) (*i*) No phase-segregated domains at the optical length scale are visible before peptide addition. Domains are evident at (*ii*) 126 s, (*iii*) 196 s, (*iv*) 293 s, (*v*) 439 s, and (*vi*) 542 s after addition. Scale bar, 30 μm. (*b*) Selected images reveal domain growth at (*i*) 90 s, (*ii*) 129 s, (*iii*) 183 s, (*iv*) 299 s, (*v*) 473 s, (*vi*) 537 s, (*vii*) 714 s, (*viii*) 741 s, and (*ix*) 788 s after peptide introduction. Scale bar, 5 μm. (*c*) Fluorescence intensity profiles of a GUV perimeter, illustrating domain growth in (*a*) (left vesicle). (*d*) Growth of the average domain area as a function of time, estimated from images in (*b*). (*e*) Fluorescence images of raft GUVs were visualized using L_d-phase (Rho-B DOPE, *red*) and L_o-phase (DP-EG10-biotin) markers. The L_o-phase marker was fluorescently visualized by binding Oregon Green 488 NeutrAvidin (*green*) introduced in the ambient bath (1 μM). (*i–iii*) Confocal slices of the equatorial plane before AH peptide addition. Scale bar, 10 μm. (*iv–vi*) 3D reconstructions generated from a Z-stack in samples incubated with 2 μM AH peptide. Scale bar, 15 μm. (*f*) Fluorescence images reveal domain formation after incubation with a mixture of 1.5 μM 5-TAMRA-AH (*red*) and 1.5 μM AH (unlabeled) peptides in raft GUVs doped with NBD-PE (*green*). (*i–iii*) Confocal fluorescence images for green, red, and merge. Scale bar, 20 μm. (*iv–vi*) 3D reconstructions generated from a Z-stack for green, red, and merge channels. Scale bar, 10 μm. (*g*) Fluorescence intensity along the vesicle perimeter, measured here in terms of the angle relative to an arbitrary point designated as 0° for the red (5-TAMRA-AH) and green (NBD-PE) channels in (*f*) (*i* and *ii*), shows colocalization of 5-TAMRA-AH in NBD-PE-rich L_d-phase domains. See text for details. To see this figure in color, go online.

presence of bright domains indicates microscopic L_d-phase fluid domains in the L_o-phase surroundings. To further ensure that the dark surroundings indeed represent the coexisting L_o phase, and to independently confirm that the observed phase separation is not induced by any interaction between the L_d-phase-partitioning probe Rho-DOPE and the peptide, we repeated the experiment using GUVs that simultaneously incorporate the L_o-phase-partitioning probe (3 mol % DP-EG10-biotin, which subsequently binds Oregon-Green-labeled NeutrAvidin; see Materials and Methods) and the L_d-phase-partitioning probe (Rho-DOPE, 1 mol %). The resulting data provide clear evidence for the in situ appearance of well-separated, coexisting L_o and L_d phases after AH incubation (Fig. 1 *e*; Movie S3). These qualitative features are fully reproducible across vesicle populations in single samples as well as in multiple independent samples ($n > 20$). They are also detectable over a range of AH peptide concentrations from 1 to 5 μM, above which the GUVs become structurally unstable, fusing to one another as well as to the confining glass surfaces.

The dynamics of this transition from an optically homogeneous state before peptide incubation to one characterized by a random distribution of microscopic circular domains (0.5–5 μm in diameter) after peptide introduction is revealed by time-lapse sequences of fluorescence images (Movies S1 and S2). These data reveal that although the L_d-phase domains fluctuate vigorously about their mean spatial locations, they do not execute long-range lateral motions within the otherwise contiguous plane of the membrane. This is not surprising, since the surrounding L_o phase is dense, which must frustrate the in-plane Brownian mobilities of the L_d-phase domains, kinetically trapping them and delaying their equilibration (40,41). Over time, however, the fluctuating neighboring domains collide and coalesce (Fig. S2), coarsening the domain sizes (Fig. 1 *d*), and become stable for extended periods of time (several tens of minutes after the introduction of AH peptide).

To determine the spatial locations of AH peptide in domain-forming GUVs, we carried out additional experiments in which a 5-TAMRA-labeled, fluorescent AH peptide was incubated with raft-forming GUVs labeled with NBD-PE (1 mol %; see Materials and Methods). The resulting data show that at the membrane surface, the peptide colocalizes almost exclusively with NBD-PE (Fig. 1, *f* and *g*; Movie S4). Because the latter partitions within the Ch-depleted L_d phase, the observed colocalization indicates that the AH peptide preferentially binds POPC in the L_d phase. Since the membrane surface is optically homogeneous before peptide binding occurs, these observations further suggest that the peptide preferentially binds the fluid-phase POPC. This in turn induces large-scale phase segregation of the L_o and L_d phases, presumably by expelling the L_o-phase-partitioning Ch and SM, and thus driving domain formation.

This preference of the AH peptide for the L_d phase is similar to what has been observed for many other membrane-binding amphipathic peptides (42–47), among which the membrane interactions of δ-lysin, a toxin secreted by the Gram-positive bacterium *Staphylococcus aureus*, displays perhaps the most striking parallel (44,48). Like the AH peptide, δ-lysin is known to bind the fluid, L_d phase in membranes containing lipid mixtures that phase separate into coexisting L_o and L_d phases.

Softening of single-component fluid GUVs induced by peptide binding

Next, we explore how AH peptide binding influences compositionally uniform membranes, which do not possess the internal compositional degrees of freedom needed to undergo phase separation. When we incubated GUVs consisting of a single fluid-phase lipid POPC ($T_m = -2°C$) with the AH peptide at comparable concentrations (1–5 μM)), we found little or no evidence for any large-scale perturbations of the membrane boundary. When the peptide concentration was increased by 2- to 10-fold (10–25 μM), a striking deformation of the membrane shape became evident. Sequences of stills selected from two representative time-lapse movies (Movies S5 and S6) are shown in Fig. 2, *ai–aix* and *bi–ix*). In the most complete case, three distinct regimes are discernible. First, in the initial phase (5–15 min) after incubation, little or no change is seen. After this lag phase, the second regime becomes apparent, which is characterized by a vigorous flickering of the membrane boundary (Fig. 2, *aiii–v* and *bi–vi*) that is noticeably more pronounced than that accounted for by thermal fluctuations alone. Characterizing this shape dynamics in terms of a shape factor for topologically closed surfaces, *S*, defined as $4\pi A/P^2$ (where *A* is the projected area and *P* is the perimeter) yields the lowest *S*-value of 0.92 (Fig. 2 *c*). Not all vesicles begin flickering at the same time, presumably reflecting a common artifact from the method used to introduce the peptide into the vesicle suspension and the stochastic nature of the transformation itself. Within a span of 2–5 min of lag phase, however, all vesicles begin to show violent flickering of the membrane boundary. This characteristic flickering of POPC GUVs after AH incubation at elevated concentrations, which reflects membrane softening, is perhaps best evaluated in terms of the membrane's elastic properties, characterized by the bending modulus (49). This is readily

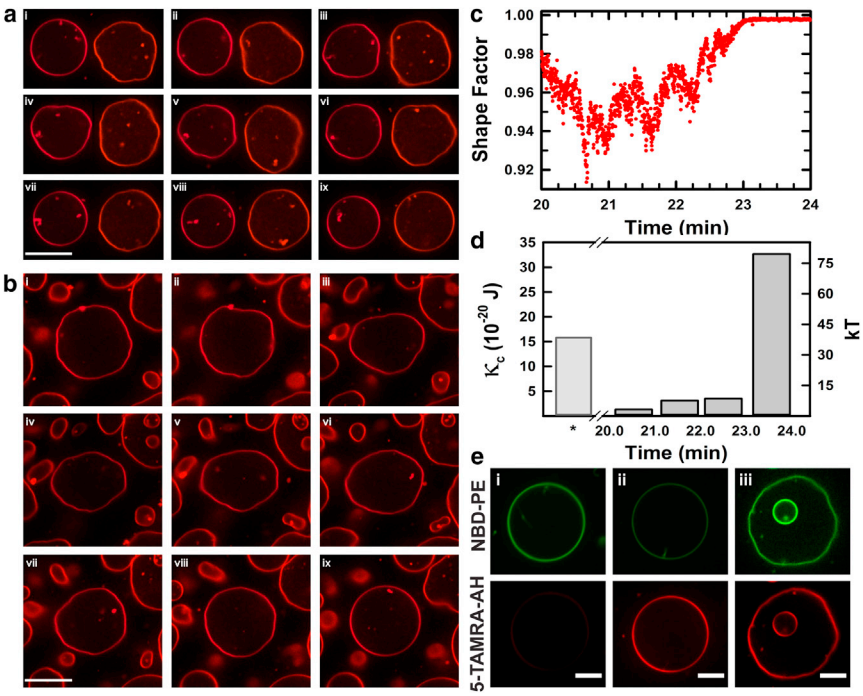

FIGURE 2 AH-peptide-induced softening of POPC GUVs. (*a* and *b*) Fluorescence images of GUVs doped with Rho-B DOPE incubated with 14 μM AH peptide. Scale bar, 20 μM. (*a*) Frame (*i*) was captured 13 min after peptide introduction. Subsequent frames in the panel (*ii–ix*) are consecutive, 20 s apart. (*b*) Frame (*i*) was captured 5.5 min after peptide introduction, and subsequent frames were acquired 30 s apart. (*c*) Shape factor plot ($S = 4\pi A/P^2$) of a vesicle cross section, showing dynamic shape changes of the GUV surface in (*b*) (middle vesicle). (*d*) Plot demonstrating dynamic softening of POPC GUVs during incubation with AH peptide, characterized by changes in the membrane bending rigidity (see text for details). (*e*) Fluorescence images of GUVs doped with NBD-PE incubated with 5-TAMRA-labeled AH peptide. Initially unbound 5-TAMRA AH (*i*) adsorbs onto the GUV membranes (*ii*) and eventually decreases the membrane rigidity (*iii*). Frames were captured at (*i*) 30 s, (*ii*) 160 s, and (*iii*) 52 min after introduction of 5-TAMRA-labeled AH peptide. Scale bars, 10 μm. To see this figure in color, go online.

achieved by estimating the angular correlation function of the relative radius fluctuations from the edge profiles to determine the flicker spectra of the membrane boundary (quantitative methods are described elsewhere (36)). When we apply these analyses using an edge-localization method developed recently by Loftus and co-workers (34) (Materials and Methods) as a function of AH peptide incubation period, we find that during the time span of the second regime of membrane flickering, the bending rigidity and corresponding membrane tension decrease monotonically, approaching vanishingly low values (Fig. 2 *d*), and ultimately climb in the third regime to near or even above the preincubation levels.

To determine the fate of the AH peptide during the above-described structural transformation at high peptide concentrations, we carried out experiments using fluorescently labeled AH peptide (Fig. 2 *e*; Movies S7 and S8). When we incubated NBD-PE (Ex/Em 463:536 nm, 1 mol %) doped POPC GUVs with 5-TAMRA-labeled (Ex/Em, 541:568 nm) AH peptides (10–35 μM; Materials and Methods), we found that the peptide accumulated at the membrane surface and remained associated during the course of the structural transformation. In selected cases in which we employed nested vesicles (i.e., vesicles-in-vesicles), we found that the labeled peptide colocalized with both the parent and the encapsulated daughter vesicle. This suggests that at least some of the peptides were able to penetrate the membrane boundary of the parent compartment, and quickly became associated with the membrane surface (rather than with the encapsulated aqueous phase) by localizing onto the interior membrane (Fig. 2 *e*).

To assess whether AH-peptide association also permeabilizes the GUV membranes, we carried out additional experiments in the presence of a fluorescent marker, NBD-glucose (28–40 μM), dissolved in the exterior buffer. As expected, the leakage marker (i.e., NBD-glucose) did not permeate unperturbed GUVs in the absence of AH peptide. Upon introduction of AH peptide (4 μM), raft-forming GUVs revealed an influx of NBD-glucose into the interior of the vesicle (Fig. 3; Movie S9): the solute permeated the raft GUVs, homogenizing the fluorescence from the NBD-glucose across the vesicular compartment. The POPC GUVs, by contrast, did not exhibit any solute influx at comparable peptide concentrations (1–5 μM), but did become permeable, before membrane flickering, at elevated peptide concentrations (10–30 μM; Fig. 3; Movie S10). Interestingly for raft membranes, the solute permeation and thus the transient membrane permeabilization coincided with the peptide-binding-induced appearance of phase-separated domains. This suggests (but does not independently establish) that peptide-induced membrane phase separation in Ch-enriched viral envelopes may provide the defect sites (50), presumably at the incipient domain boundaries, facilitating membrane permeabilization (51). This is consistent with models of stable pore formation in membranes by the association of amphipathic peptides (52,53). Here, the translocation of the peptide across the bilayer, presumably through transient pores, serves to stretch both leaflets, which in turn stabilizes the pores above a critical strain.

Taken together, the above results substantiate that the AH peptide discriminates between membrane compositions. The GUV membranes composed of raft-forming lipid

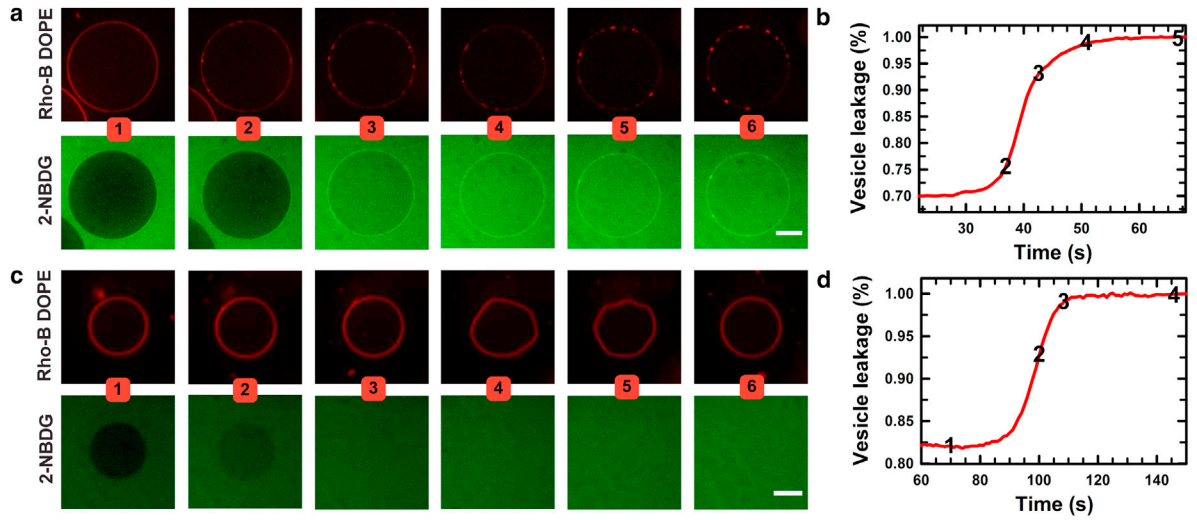

FIGURE 3 Leakage assays. Permeabilization of GUV membranes was measured by monitoring the relative fluorescence intensity of 2-NBD-labeled glucose (*green*) inside and outside the vesicle after incubation with the AH peptide. (*a*) Fluorescence image sequence of GUVs consisting of equimolar concentrations of POPC, Ch, and SM doped with Rho-B, upon incubation with 4 μM AH peptide. Images were taken at 1) 607 s, 2) 637 s, 3) 645 s, 4) 652 s, 5) 667 s, and 6) 682 s after peptide addition, corresponding to quantitative leakage values in (*b*). Scale bar, 10 μm. (*b*) Normalized fluorescence intensity profile for leakage of 2-NBD-labeled glucose into the raft GUV in (*a*). (*c*) Fluorescence image sequence of a POPC GUV doped with Rho-B after incubation with 10 μM AH peptide (at 20 s). Images were taken at 1) 70 s, 2) 100 s, 3) 107 s, 4) 146 s, 5) 166 s, and 6) 205 s, corresponding to quantitative leakage values in (*d*). Scale bar, 10 μm. (*d*) Normalized fluorescence intensity profile for leakage of 2-NBDG into a POPC GUV. To see this figure in color, go online.

mixtures undergo lateral segregation of membrane components, producing optically resolved microscopic domains and concomitant permeabilization, whereas single-component fluid GUV membranes reveal little or no perturbations at comparable peptide concentrations. At elevated peptide concentrations, however, compositionally uniform POPC GUVs display vigorous flickering of the membrane boundary, confirming peptide association with the POPC lipid and vesicular permeabilization, which precedes it.

This composition-dependent mechanism of action for the AH peptide can be reconciled in terms of a unifying mechanistic picture. The softening of single-component POPC lipid membranes can be understood to be a direct consequence of membrane-parallel orientation of the AH peptide at the lipid surface (11). The interfacial peptide association, with its hydrophobic face embedded in the membrane hydrophobic core, locally increases the separation between polar lipid headgroups in the proximal monolayer, resulting in both the perturbation of chain packing (53,54) and the creation of an area difference between the two leaflets constituting the membrane bilayer (55,56). Together, these factors lower the energy cost for the creation of local and mobile hotspots for curvature generation (49), giving rise to large-scale, global membrane undulations and a decrease in the membrane bending rigidity, in the regime of low peptide-to-lipid molar ratios below the threshold for stable pore formation (54) such as observed here.

By contrast, when a single-component, fluid membrane is substituted by a multicomponent, raft-forming one (e.g., as found in viral membranes targeted by the AH peptide), out-of-plane membrane boundary fluctuations are suppressed, and replaced by membrane dynamics characterized by an in-plane segregation of membrane components. Two major well-understood biophysical mechanisms must act in concert to drive the observed domain formation. First, because AH peptide binds preferentially to the POPC component, and because in pure POPC membranes AH binding dramatically lowers the membrane bending rigidity (presumably by thinning, disordering, and fluidizing the bilayer; see above), the corresponding amplification in the hydrophobic mismatch between peptide-binding POPC and Ch-sequestering SM might provide the force necessary to drive domain formation (57). Second, the segregation of peptide-bound POPC would necessarily alter the molar ratios of free lipids in favor of phase separation in the phase diagram. The minimization of the line tension between the incipient L_d and L_o phases would then explain the subsequent coalescence of domains (57). Based on the above observations, it seems plausible that the anchoring of the AH domain of NS5A at the ER membrane might similarly lead to the accumulation of Ch-enriched raft domains in situ. This then suggests a heretofore unappreciated role of NS5A in providing a platform for the tight association of viral factors with cytoplasmic membranes, as well as with select components of the cytoplasmic membranes (i.e., Ch-enriched raft compositions), for subsequent budding of the nascent virion (58).

The molecular origins of the binding preference of AH peptides, and whether AH peptides have an intrinsic affinity for specific lipid headgroups that partition within the L_d phase, are neither independently known nor established by the results presented here. Like several other membrane-binding amphipathic peptides (42–47) (among which δ-lysin, a toxin secreted by the Gram-positive bacterium *S. aureus*, is perhaps the most striking case (44,48)), the phase-sensitive binding of AH peptides may be due to a combination of subtle factors rather than to a dependence on the headgroup properties alone. Some examples of mechanisms that have previously been reported to confer a phase preference to peptide (or protein) binding to membranes include headgroup composition, sensitivity to local packing and lateral fluidity, and affinity (or lack thereof) for domain-partitioning Ch (59). Indeed, similar mechanisms are operative in conferring antimicrobial activity to a variety of naturally occurring amphipathic AH peptides, such as δ-lysin, melittin, and magainin (44,49,52).

From the viewpoint of membrane physical chemistry, it appears instructive to appreciate that this protein-binding-induced phase separation exemplifies the extreme responsiveness of membrane structure and organization to external perturbations. Indeed, the well-known phenomenon of critical fluctuations near a critical point provides an extraordinary example of how even weak thermal fluctuations can transiently drive membrane reorganization (60). More generally, it has been demonstrated experimentally and is well understood theoretically that these collective demixing (or mixing) effects extend far away from the critical point (along any order parameter direction), causing membrane mixtures to exhibit a rather high sensitivity to external perturbations. This perhaps is best illustrated by experiments that revealed strong enhancements in membrane demixing in the presence of external electric fields (61), and, more recently, in membranes subjected to osmotic differentials (62), suggesting that there is a very broad region of phase space where effects such as protein binding may produce large, collective changes in membrane organization in situ.

Does size matter? Because viral envelopes are topologically closed nanometer-scale containers for the viral genome, we asked whether viral size also plays a role in determining the virocidal activity of the AH peptide. Indeed, previous studies using surface-immobilized small unilamellar vesicles (25–100 nm, prepared by sonication) and LUVs (nominally 100 nm in diameter, prepared by extrusion) have shown that the AH peptide is membrane lytic in a size-dependent manner in the limit of nanometer-scale diameters (60–150 nm vesicles rupture, but larger ones ($\geq$200 nm) do not) (63). To assess whether size and composition couple in determining the specificity of the AH peptide for viral membranes over larger, microscopic cell membranes, we conducted model competition assays (Fig. 4 *a*). Here, the AH

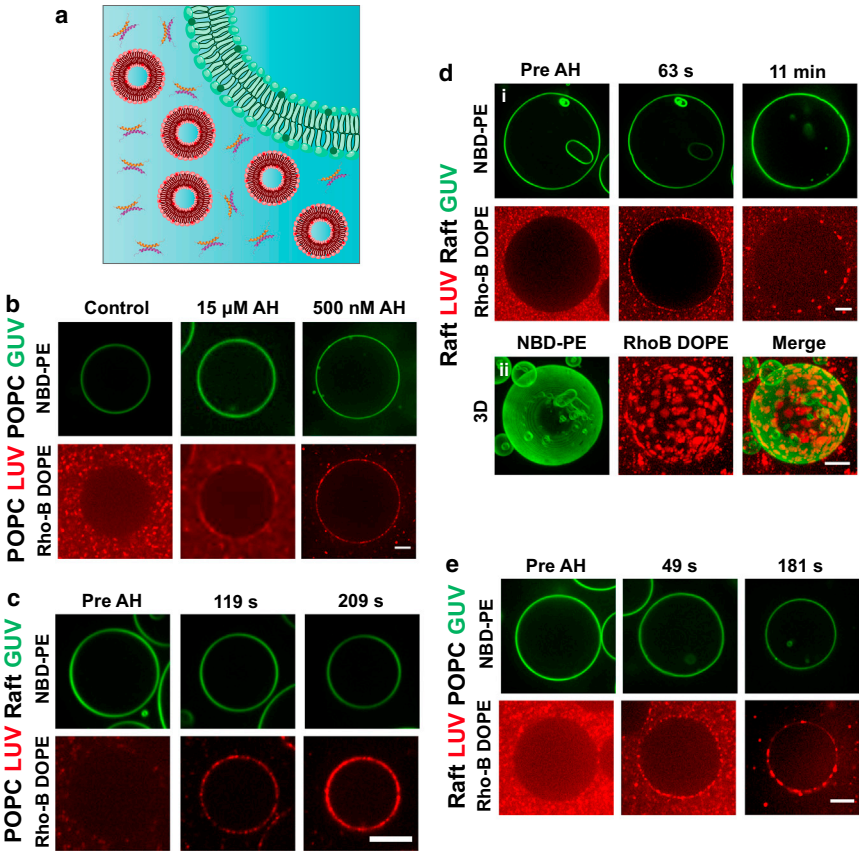

FIGURE 4 POPC and raft GUV-LUV competition assays. GUVs and LUVs consisting of either raft-forming (equimolar POPC, egg-SM, and Ch) or POPC lipids incubated with the AH peptide are shown. The four permutations of vesicle size (GUV or LUV) and composition (raft or POPC) were tested. (*a*) Cartoon depicting GUV and LUV competition assays with AH peptide. (*b–e*) Selected fluorescence images of GUVs doped with NBD-PE, and LUVs doped with Rho-B DOPE, before and after incubation with AH peptide. (*b*) GUV/LUV: POPC/POPC, incubated at 500 nM and 15 μM AH peptide. (*c*) GUV/LUV: raft/POPC. Postincubation images were taken at 119 s and 209 s after addition of 1 μM AH peptide. (*d*) (*i*) GUV/LUV: raft/raft. Postincubation images were taken at 63 s and 10 min with 1 μM AH peptide. (*ii*) Maximum Z-projection constructed from a Z-stack after 5 min of incubation with 1 μM AH. (*e*) GUV/LUV: POPC/raft. Postincubation images were taken at 69 s and 201 s after addition 2 μM AH peptide. Scale bar, 10 μm. To see this figure in color, go online.

peptide is incubated with a mixed populations consisting of LUVs (~100 nm) and GUVs (10–30 μm). We used both single-component POPC and raft-forming lipid mixtures (Materials and Methods), spanning all four permutations. The results summarized in Fig. 4, *b–e* (also see Materials and Methods; Movies S11, S12, and S13), reveal a number of noteworthy features. First, we find that the presence of LUVs (of any composition) strikingly inhibits the effects of the AH peptide on GUVs in the absence of LUVs: POPC GUVs do not soften and raft-forming GUVs remain uniform, untextured by domains. Because in many experiments the concentrations of GUVs and LUVs we used are expected to be comparable, assuming that all lipids participate in vesicle formation, it seems likely that our results reflect a size-dependent AH peptide interaction. We note, however, that the lack of quantitative control over lipid areas of GUVs and LUVs (because of inherent variabilities in the formation procedures used) precludes us from making definitive inferences. Second, the enhancement of fluorescence due to probes at the GUV boundary indicates that the lipids from LUVs are trafficked to the GUV boundary upon AH incubation. When the LUVs consist of POPC alone, the trafficked membrane from the LUVs appears to rather uniformly decorate the GUV surface, consistent with the docking of unruptured LUVs (Fig. 4, *b* and *c*). By contrast, when the trafficked LUVs contain raft-forming lipid mixtures, the LUV components produce large, microscopic features suggesting integration of ruptured LUVs with the GUV membrane (Fig. 4, *d* and *e*). Third, analyses of FRAP measurements indicate a drastic reduction in long-range lateral diffusivity of fluorescent lipid probes in all cases, suggesting that the lipids delivered by LUVs do not diffuse freely (Materials and Methods; Fig. S3; Movies S14, S15, S16, and S17). For instance, in the case of POPC/POPC GUV/LUV, the lateral diffusion constant drops from ~9.5 $\mu m^2/s$ to ~2 $\mu m^2/s$ (Figs. 5 and S3). This is consistent with the docking of peptide-associated LUVs at the membrane surface of the GUV. At present, the biological significance of this peptide-mediated adhesion and/or fusion of large vesicles to the GUV surface is unclear.

In summary, the results presented here establish that the membrane interactions of the viral-coded AH peptide are strongly modulated by the compositions of the interacting membranes. Because the membranes of viruses inhibited by the AH peptide are invariably enriched in raft-forming Ch and SM and possess intrinsic positive curvatures, we infer that the broad-spectrum virocidal properties of the AH peptide stem from its ability to preferentially bind and destabilize the virion (10) due to the combined effects of size and composition. Moreover, the observed peptide-binding-induced molecular rearrangements suggest how the association of NS5A with the ER membrane might locally

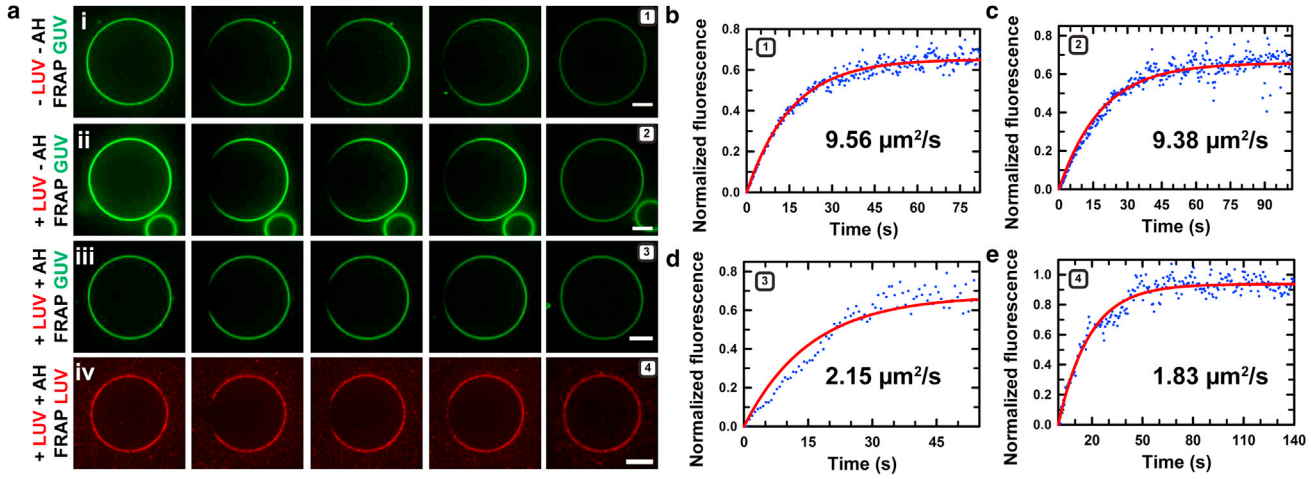

FIGURE 5 Characterization of membrane fluidity in competition assays. Measurements of the lateral diffusion constants of fluorescently labeled probe lipids preinserted into GUVs or delivered by interacting LUVs, using time-lapse images from FRAP experiments. (*a*) Selected fluorescence image sequences of NBD-labeled POPC GUVs (*green*) and material decorating the GUV surface delivered by Rho-B-labeled POPC LUVs (*red*) from the surrounding bulk. Fluorescence was monitored before and directly after bleaching, until complete recovery was achieved. (*i–iii*) GUV fluorescent probe (*green*) recovery in (*i*) the absence of LUVs or AH peptide (prebleach, 0 s, 1 s, 2 s, 100 s after bleaching; Movie S4), (*ii*) the presence of LUVs without incubation with AH peptide (prebleach, 0 s, 1 s, 2 s, 60 s; Movie S15), and (*iii*) the presence of LUVs and after incubation with 2 μM AH peptide (prebleach, 0 s, 2 s, 5 s, 50 s; Movie S16). (*iv*) LUV-derived material with Rho-B (*red*) decorating the GUV, showing recovery after addition of and incubation with 2 μM AH peptide (prebleach, 0 s, 2 s, 5 s, 60 s; Movie S17). Scale bars, 10 μm. (*b–e*) Normalized fluorescence recovery curves for FRAP experiments: (*b*) (e-i), $D = 9.56\ \mu m^2/s$; (*c*) (e-ii), $D = 9.38\ \mu m^2/s$; (*d*) (e-iii), $D = 2.15\ \mu m^2/s$; and (*e*) (e-iv), $D = 1.83\ \mu m^2/s$. To see this figure in color, go online.

enhance the concentrations of L_o-phase-forming lipids, whose subsequent budding (and fission) may aid in the formation of vesicles that become part of the membranous web where RNA replication is thought to occur (23,25).

SUPPORTING MATERIAL

Three figures and seventeen movies are available at http://www.biophysj.org/biophysj/supplemental/S0006-3495(15)01215-1.

AUTHOR CONTRIBUTIONS

N.-J.C. and A.N.P. conceived the project and designed experiments. J.M.H. and D.L.G. performed all GUV experiments. D.Y.S., S.R.T., and J.J. provided reagents and contributed to data analyses. All co-authors (J.M.H., D.L.G., S.R.T., J.J., M.C.K., D.Y.S., J.T.G., B.L., N.J.C., and A.N.P.) contributed to data interpretation and manuscript revisions, and agreed on the final contents of the manuscript.

ACKNOWLEDGMENTS

We thank A. Loftus and R. Parthasarathy for sharing their MATLAB code for shape fluctuation analyses and estimation of membrane bending rigidities. We also thank T. Allen for suggestions and illuminating discussions.

This work was supported by a grant from the Biomolecular Materials Program, Division of Materials Science and Engineering, Basic Energy Sciences, U.S. Department of Energy under award No. DE-FG02-04ER46173 (A.N.P.). N.J.C. received support from the National Research Foundation (NRFF2011-01) and the National Medical Research Council (NMRC/CBRG/0005/2012). N.-J.C., A.N.P., and B.L. received additional support from Nanyang Technological University through the Centre for Biomimetic Sensor Science. D.Y.S. was supported by the Materials Science and Engineering Division, Office of Basic Energy Sciences, U.S. Department of Energy (KC0203010). Sandia National Laboratories is a multiprogram laboratory managed and operated by Sandia Corporation, a wholly owned subsidiary of Lockheed Martin Corporation, for the U.S. Department of Energy's National Nuclear Security Administration under contract DE-AC04-94AL85000. D.L.G. was partially supported by an industry/campus-supported fellowship under the Training Program in Biomolecular Technology (T32-GM008799) at the University of California, Davis. Spinning-disk confocal fluorescence microscopy experiments were performed at the Molecular & Cell Biology Imaging Facility at UC Davis.

REFERENCES

1. Ma-Lauer, Y., J. Lei, …, A. von Brunn. 2012. Virus-host interactomes—antiviral drug discovery. *Curr. Opin. Virol.* 2:614–621.
2. Nagy, P. D., and J. Pogany. 2012. The dependence of viral RNA replication on co-opted host factors. *Nat. Rev. Microbiol.* 10:137–149.
3. Chernomordik, L. V., J. Zimmerberg, and M. M. Kozlov. 2006. Membranes of the world unite! *J. Cell Biol.* 175:201–207.
4. Chernomordik, L. V., S. S. Vogel, …, J. Zimmerberg. 1993. Lysolipids reversibly inhibit Ca(2+)-, GTP- and pH-dependent fusion of biological membranes. *FEBS Lett.* 318:71–76.
5. St Vincent, M. R., C. C. Colpitts, …, L. M. Schang. 2010. Rigid amphipathic fusion inhibitors, small molecule antiviral compounds against enveloped viruses. *Proc. Natl. Acad. Sci. USA.* 107:17339–17344.
6. Wolf, M. C., A. N. Freiberg, …, B. Lee. 2010. A broad-spectrum antiviral targeting entry of enveloped viruses. *Proc. Natl. Acad. Sci. USA.* 107:3157–3162.
7. Kilby, J. M., S. Hopkins, …, M. S. Saag. 1998. Potent suppression of HIV-1 replication in humans by T-20, a peptide inhibitor of gp41-mediated virus entry. *Nat. Med.* 4:1302–1307.
8. Lamarre, D., P. C. Anderson, …, M. Llinàs-Brunet. 2003. An NS3 protease inhibitor with antiviral effects in humans infected with hepatitis C virus. *Nature.* 426:186–189.

9. Lambert, D. M., S. Barney, …, S. R. Petteway, Jr. 1996. Peptides from conserved regions of paramyxovirus fusion (F) proteins are potent inhibitors of viral fusion. *Proc. Natl. Acad. Sci. USA.* 93:2186–2191.
10. Cheng, G., A. Montero, …, F. V. Chisari. 2008. A virocidal amphipathic alpha-helical peptide that inhibits hepatitis C virus infection in vitro. *Proc. Natl. Acad. Sci. USA.* 105:3088–3093.
11. Penin, F., V. Brass, …, D. Moradpour. 2004. Structure and function of the membrane anchor domain of hepatitis C virus nonstructural protein 5A. *J. Biol. Chem.* 279:40835–40843.
12. Eckert, D. M., and P. S. Kim. 2001. Mechanisms of viral membrane fusion and its inhibition. *Annu. Rev. Biochem.* 70:777–810.
13. Lindenbach, B. D., and C. M. Rice. 2005. Unravelling hepatitis C virus replication from genome to function. *Nature.* 436:933–938.
14. Cho, N. J., K. H. Cheong, …, J. S. Glenn. 2007. Binding dynamics of hepatitis C virus' NS5A amphipathic peptide to cell and model membranes. *J. Virol.* 81:6682–6689.
15. Cho, N. J., H. Dvory-Sobol, …, J. S. Glenn. 2009. Mechanism of an amphipathic alpha-helical peptide's antiviral activity involves size-dependent virus particle lysis. *ACS Chem. Biol.* 4:1061–1067.
16. Elazar, M., K. H. Cheong, …, J. S. Glenn. 2003. Amphipathic helix-dependent localization of NS5A mediates hepatitis C virus RNA replication. *J. Virol.* 77:6055–6061.
17. Simons, K., and E. Ikonen. 1997. Functional rafts in cell membranes. *Nature.* 387:569–572.
18. Aizaki, H., K. Morikawa, …, T. Suzuki. 2008. Critical role of virion-associated cholesterol and sphingolipid in hepatitis C virus infection. *J. Virol.* 82:5715–5724.
19. Manié, S. N., S. de Breyne, …, D. Gerlier. 2000. Measles virus structural components are enriched into lipid raft microdomains: a potential cellular location for virus assembly. *J. Virol.* 74:305–311.
20. Chang, T. H., J. Segovia, …, S. Bose. 2012. Cholesterol-rich lipid rafts are required for release of infectious human respiratory syncytial virus particles. *Virology.* 422:205–213.
21. Aloia, R. C., H. Tian, and F. C. Jensen. 1993. Lipid composition and fluidity of the human immunodeficiency virus envelope and host cell plasma membranes. *Proc. Natl. Acad. Sci. USA.* 90:5181–5185.
22. Chazal, N., and D. Gerlier. 2003. Virus entry, assembly, budding, and membrane rafts. *Microbiol. Mol. Biol. Rev.* 67:226–237.
23. Moradpour, D., F. Penin, and C. M. Rice. 2007. Replication of hepatitis C virus. *Nat. Rev. Microbiol.* 5:453–463.
24. Ferraris, P., E. Blanchard, and P. Roingeard. 2010. Ultrastructural and biochemical analyses of hepatitis C virus-associated host cell membranes. *J. Gen. Virol.* 91:2230–2237.
25. Miller, S., and J. Krijnse-Locker. 2008. Modification of intracellular membrane structures for virus replication. *Nat. Rev. Microbiol.* 6:363–374.
26. Romero-Brey, I., A. Merz, …, R. Bartenschlager. 2012. Three-dimensional architecture and biogenesis of membrane structures associated with hepatitis C virus replication. *PLoS Pathog.* 8:e1003056.
27. Hijikata, M., H. Mizushima, …, K. Shimotohno. 1993. Proteolytic processing and membrane association of putative nonstructural proteins of hepatitis C virus. *Proc. Natl. Acad. Sci. USA.* 90:10773–10777.
28. Momin, N., S. Lee, …, D. Y. Sasaki. 2015. Designing lipids for selective partitioning into liquid ordered membrane domains. *Soft Matter.* 11:3241–3250.
29. Angelova, M. I., and D. S. Dimitrov. 1986. Liposome electroformation. *Faraday Discuss.* 81:303.
30. Morales-Penningston, N. F., J. Wu, …, G. W. Feigenson. 2010. GUV preparation and imaging: minimizing artifacts. *Biochim. Biophys. Acta.* 1798:1324–1332.
31. Mayer, L. D., M. J. Hope, and P. R. Cullis. 1986. Vesicles of variable sizes produced by a rapid extrusion procedure. *Biochim. Biophys. Acta.* 858:161–168.
32. Manneville, J. B., J. F. Casella, …, B. Goud. 2008. COPI coat assembly occurs on liquid-disordered domains and the associated membrane deformations are limited by membrane tension. *Proc. Natl. Acad. Sci. USA.* 105:16946–16951.
33. Kang, M., C. A. Day, …, E. DiBenedetto. 2012. Simplified equation to extract diffusion coefficients from confocal FRAP data. *Traffic.* 13:1589–1600.
34. Loftus, A. F., S. Noreng, …, R. Parthasarathy. 2013. Robust measurement of membrane bending moduli using light sheet fluorescence imaging of vesicle fluctuations. *Langmuir.* 29:14588–14594.
35. Henriksen, J., A. C. Rowat, and J. H. Ipsen. 2004. Vesicle fluctuation analysis of the effects of sterols on membrane bending rigidity. *Eur. Biophys. J.* 33:732–741.
36. Méléard, P., T. Pott, …, J. H. Ipsen. 2011. Advantages of statistical analysis of giant vesicle flickering for bending elasticity measurements. *Eur Phys J E Soft Matter.* 34:116.
37. Veatch, S. L., and S. L. Keller. 2005. Miscibility phase diagrams of giant vesicles containing sphingomyelin. *Phys. Rev. Lett.* 94:148101.
38. Baumgart, T., G. Hunt, …, G. W. Feigenson. 2007. Fluorescence probe partitioning between Lo/Ld phases in lipid membranes. *Biochim. Biophys. Acta.* 1768:2182–2194.
39. Heberle, F. A., J. Wu, …, G. W. Feigenson. 2010. Comparison of three ternary lipid bilayer mixtures: FRET and ESR reveal nanodomains. *Biophys. J.* 99:3309–3318.
40. Kaizuka, Y., and J. T. Groves. 2004. Structure and dynamics of supported intermembrane junctions. *Biophys. J.* 86:905–912.
41. Samsonov, A. V., I. Mihalyov, and F. S. Cohen. 2001. Characterization of cholesterol-sphingomyelin domains and their dynamics in bilayer membranes. *Biophys. J.* 81:1486–1500.
42. Abraham, T., R. N. Lewis, …, R. N. McElhaney. 2005. Isothermal titration calorimetry studies of the binding of a rationally designed analogue of the antimicrobial peptide gramicidin s to phospholipid bilayer membranes. *Biochemistry.* 44:2103–2112.
43. Epand, R. M., R. F. Epand, …, G. M. Anantharamaiah. 2004. An apolipoprotein AI mimetic peptide: membrane interactions and the role of cholesterol. *Biochemistry.* 43:5073–5083.
44. Pokorny, A., and P. F. F. Almeida. 2005. Permeabilization of raft-containing lipid vesicles by delta-lysin: a mechanism for cell sensitivity to cytotoxic peptides. *Biochemistry.* 44:9538–9544.
45. Gandhavadi, M., D. Allende, …, T. J. McIntosh. 2002. Structure, composition, and peptide binding properties of detergent soluble bilayers and detergent resistant rafts. *Biophys. J.* 82:1469–1482.
46. McHenry, A. J., M. F. M. Sciacca, …, A. Ramamoorthy. 2012. Does cholesterol suppress the antimicrobial peptide induced disruption of lipid raft containing membranes? *Biochim. Biophys. Acta.* 1818: 3019–3024.
47. Zhong, J., C. Yang, …, Y. Sha. 2009. Effects of lipid composition and phase on the membrane interaction of the prion peptide 106-126 amide. *Biophys. J.* 96:4610–4621.
48. Pokorny, A., L. E. Yandek, …, P. F. F. Almeida. 2006. Temperature and composition dependence of the interaction of delta-lysin with ternary mixtures of sphingomyelin/cholesterol/POPC. *Biophys. J.* 91:2184–2197.
49. Bouvrais, H., P. Méléard, …, J. H. Ipsen. 2008. Softening of POPC membranes by magainin. *Biophys. Chem.* 137:7–12.
50. Lawaczeck, R., M. Kainosho, …, S. I. Chan. 1975. Effects of structural defects in sonicated phospholipid vesicles on fusion and ion permeability. *Nature.* 256:584–586.
51. Kanehisa, M. I., and T. Y. Tsong. 1978. Cluster model of lipid phase-transitions with application to passive permeation of molecules and structure relaxations in lipid bilayers. *J. Am. Chem. Soc.* 100:424–432.
52. Lee, M. T., T. L. Sun, …, H. W. Huang. 2013. Process of inducing pores in membranes by melittin. *Proc. Natl. Acad. Sci. USA.* 110:14243–14248.
53. Hristova, K., C. E. Dempsey, and S. H. White. 2001. Structure, location, and lipid perturbations of melittin at the membrane interface. *Biophys. J.* 80:801–811.

54. Lee, J.-H., S.-M. Choi, …, S. R. Kline. 2010. Thermal fluctuation and elasticity of lipid vesicles interacting with pore-forming peptides. *Phys. Rev. Lett.* 105:038101.

55. Sheetz, M. P., and S. J. Singer. 1974. Biological membranes as bilayer couples. A molecular mechanism of drug-erythrocyte interactions. *Proc. Natl. Acad. Sci. USA.* 71:4457–4461.

56. Svetina, S., and B. Zeks. 1985. Bilayer couple as a possible mechanism of biological shape formation. *Biomed. Biochim. Acta.* 44:979–986.

57. Akimov, S. A., P. I. Kuzmin, …, F. S. Cohen. 2007. Lateral tension increases the line tension between two domains in a lipid bilayer membrane. *Phys. Rev. E Stat. Nonlin. Soft Matter Phys.* 75:011919.

58. Bartenschlager, R., and V. Lohmann. 2000. Replication of hepatitis C virus. *J. Gen. Virol.* 81:1631–1648.

59. Pokorny, A., E. M. Kilelee, …, P. F. F. Almeida. 2008. The activity of the amphipathic peptide delta-lysin correlates with phospholipid acyl chain structure and bilayer elastic properties. *Biophys. J.* 95:4748–4755.

60. Veatch, S. L., O. Soubias, …, K. Gawrisch. 2007. Critical fluctuations in domain-forming lipid mixtures. *Proc. Natl. Acad. Sci. USA.* 104:17650–17655.

61. Groves, J. T., S. G. Boxer, and H. M. McConnell. 1998. Electric field-induced critical demixing in lipid bilayer membranes. *Proc. Natl. Acad. Sci. USA.* 95:935–938.

62. Oglęcka, K., P. Rangamani, …, A. N. Parikh. 2014. Oscillatory phase separation in giant lipid vesicles induced by transmembrane osmotic differentials. *eLife.* 3:e03695.

63. Jackman, J. A., G. H. Zan, …, N.-J. Cho. 2013. Rupture of lipid vesicles by a broad-spectrum antiviral peptide: influence of vesicle size. *J. Phys. Chem. B.* 117:16117–16128.

SUPPORTING MATERIAL

Cholesterol-enriched microdomain formation induced by viral-encoded, membrane active amphipathic peptide

Joshua M. Hanson[1,§], Douglas L. Gettel[2,§], Seyed R. Tabaei[3,4], Joshua Jackman[3,4], Min Chul Kim[3,4], Darryl Y. Sasaki[5], Jay T. Groves[6], Bo Liedberg[3,4], Nam-Joon Cho*[3,4,7], and Atul N. Parikh*[1,2,3,4,8]

[1]Biophysics Graduate Group, University of California, Davis, California 95616 USA
[2]Department of Chemical Engineering & Materials Science, University of California, Davis, California 95616 USA
[3]Centre for Biomimetic Sensor Science, Nanyang Technological University, 50 Nanyang Drive 637553, Singapore
[4]School of Materials Science and Engineering, Nanyang Technological University, 50 Nanyang Ave 637459, Singapore
[5]Biotechnology and Bioengineering Dept., Sandia National Laboratories, Livermore, California 94551 USA
[6]Chemistry Department, University of California, Berkeley, California 94720 USA and Mechanobiology Institute, National University of Singapore, Singapore 117411
[7]School of Chemical and Biomedical Engineering, Nanyang Technological University, 62 Nanyang Drive 637459, Singapore
[8]Department of Biomedical Engineering, University of California, Davis, California 95616 USA

[§] J.M.H. and D.L.G. contributed equally.

Correspondence:
Atul N. Parikh, Departments of Biomedical Engineering and Chemical Engineering & Materials Science, University of California, Davis, California 95616 USA, Phone: +1 (530) 304-7523, anparikh@ucdavis.edu

Keywords: antiviral mechanisms | viral replication mechanisms | membrane-peptide interactions | giant lipid vesicles | phase separation

SUPPORTING FIGURES & LEGENDS

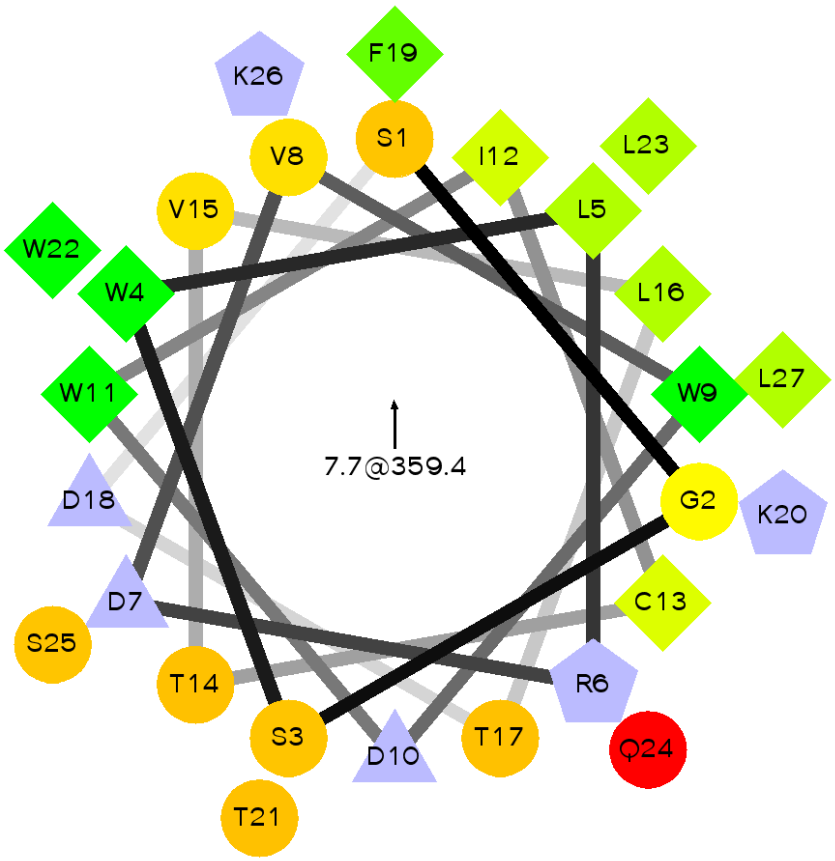

Fig. S1. Helical Wheel Projection of AH Peptide. AH Peptide sequence of amino acids: SGSWLRDVWDWICTVLTDFKTWLQSKL. A helical wheel projection showing hydrophilic residues (circles), hydrophobic residues (diamonds), potentially negatively charged residues (triangles), and potentially positively charged residues (pentagons). Hydrophobicity is color coded: most hydrophobic residue (green), with amount of green decreasing proportionally to the hydrophobicity; zero hydrophobicity (yellow); hydrophilic residues (red); and potentially charged residues (light blue). Projection was produced using a program from http://rzlab.ucr.edu created by Don Armstrong and Raphael Zidovetzki. Version: Id: wheel.pl,v 1.4 2009-10-20 21:23:36 don Exp.

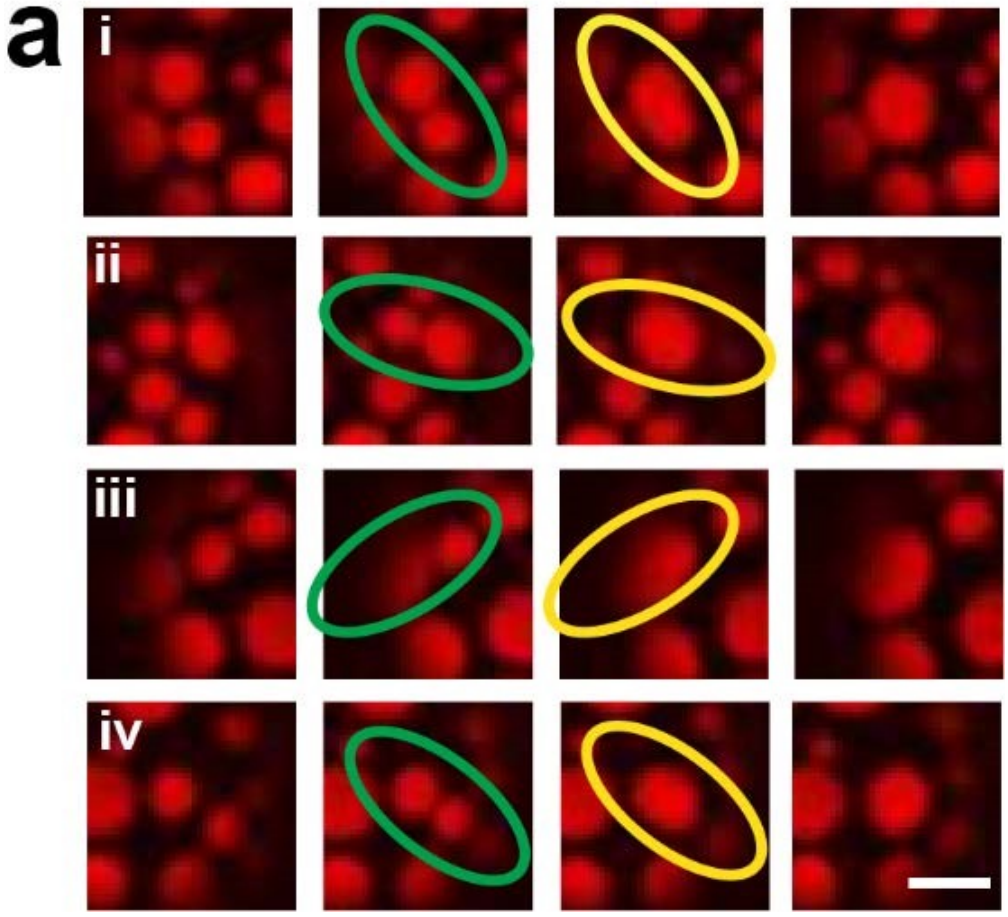

Fig. S2. Peptide-mediated domain coalescence. Selected frames from time-lapse fluorescence images of electroformed GUVs consisting of POPC/ Sphingomyelin/ Cholesterol/ Rho-B DOPE (33/33/33/1) upon incubation with 5 µM AH peptide (See main narrative for additional details). The sequences, i through iv above, illustrate domain growth through domain-domain coalescence at four different instances in a single experiment. Scale Bar, 5 µm.

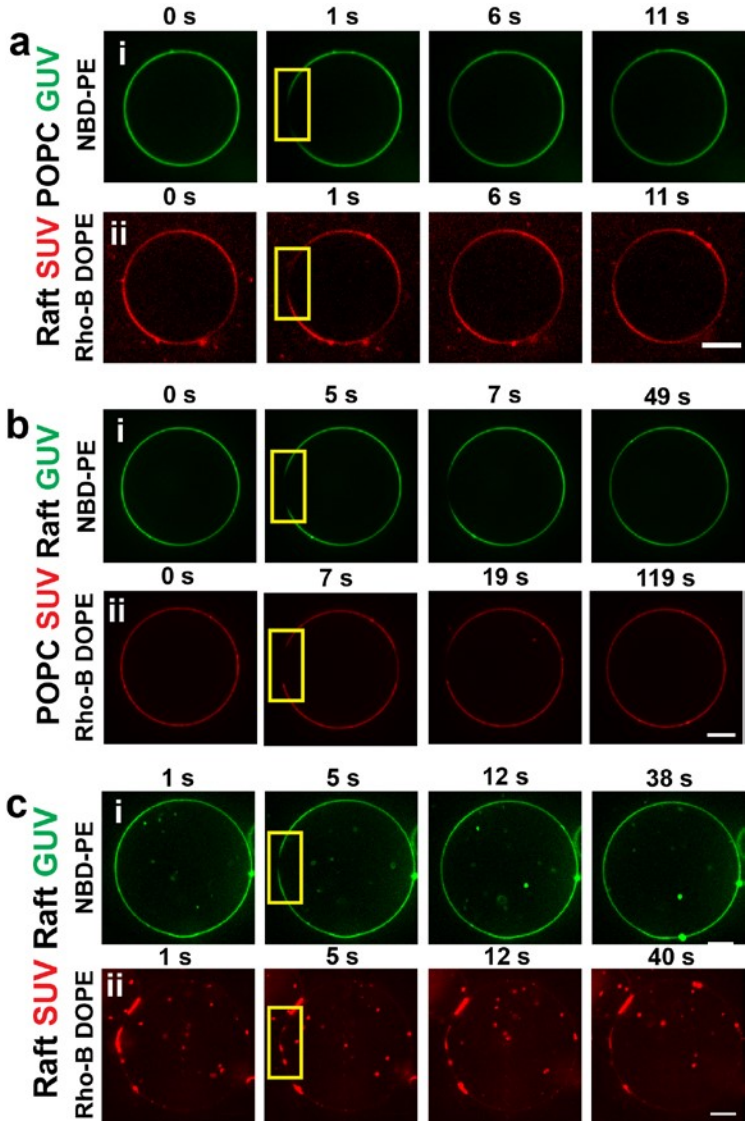

Fig. S3. Competition Assay FRAP Experiments. Selected fluorescence images of FRAP experiments using GUVs and SUVs consisting of either raft [POPC/Sphingomyelin/Cholesterol (33/33/33)] or POPC membranes (as indicated) incubated with 1 uM AH peptide. The remaining three permutations of vesicle size, GUV or SUV, and composition, Raft or POPC, are tested in addition to previously shown GUV/SUV POPC/POPC (see **Fig. 5**). **a,** GUV/SUV POPC/raft (i) bleach NBD-PE, images taken at 0 s, 1 s, 6 s, 11 s (ii) bleach Rho-B DOPE, images taken at 0 s, 1 s, 6 s, 11 s. **b,** GUV/SUV raft/POPC (i) bleach NBD-PE, images taken at 0 s, 5 s, 7s, 49 s (ii) bleach Rho-B DOPE, images taken at 0 s, 7 s, 19 s, 119 s. **c,** GUV/SUV raft/raft (i) bleach NBD-PE with images taken at 1 s, 5 s, 12 s, 38 s (ii) bleach Rho-B DOPE with images taken at 1 s, 5 s,12 s, 40 s. Yellow boxes highlight bleached regions. Scale Bars, 10 µm.

SUPPORTING MOVIE LEGENDS

Movie S1. A representative example (1 of 2) of time-lapse sequence of fluorescence images, acquired using spinning disk confocal fluorescence microscopy, of electroformed GUVs consisting of **POPC/Sphingomyelin/Cholesterol/Rhodamine-B DOPE (33/33/33/1)** containing 300 mM sucrose inside and 300 mM glucose outside duing incubation with **5 μM AH Peptide**. Scale bar = 30 μM.

Movie S2. A representative example (2 of 2) of time-lapse sequence of fluorescence images, acquired using spinning disk confocal fluorescence microscopy, of electroformed GUVs consisting of **POPC/Sphingomyelin/Cholesterol/Rhodamine-B DOPE (33/33/33/1)** containing 300 mM sucrose inside and 300 mM glucose outside duing incubation with **5 μM AH Peptide**. Scale bar = 30 μM.

Movie S3. A time-lapse sequence of fluorescence images, acquired using spinning disk confocal fluorescence microscopy, of electroformed GUVs consisting of **POPC/Sphingomyelin/Cholesterol/DP-EG10-Biotin/Rhodamine-B DOPE (32/32/32/3/1)** containing 300 mM sucrose in the vesicle interior and a mixture of 300 mM glucose (92%) and 1X PBS pH 7.2 (8%) in the exterior bath. After incubation with **2 μM AH** peptide, vesicles were then incubated with **1 μM Oregon Green 488 Neutravidin**, which binds and aids in the visualization of the DP-EG10-Biotin. Scale bar = 20 μM.

Movie S4. A representative time-lapse sequence of fluorescence images, acquired using spinning disk confocal fluorescence microscopy, of Electroformed GUVs consisting of **POPC/Sphingomyelin/Cholesterol/NBD-PE (33/33/33/1)** containing 300 mM sucrose inside and 300 mM glucose outside. Vesicles were incubated with a mixture of 1.5 µM **5-TAMRA-labeled AH peptide** and 1.5 µM AH peptide (1.5 + 1.5 = **3 µM** total). Scale bar = 30 µM.

Movie S5. A typical example (1 of 2) of time-lapse sequence of fluorescence images, acquired using spinning disk confocal fluorescence microscopy, of electroformed GUVs consisting of **POPC/Rhodamine-B DOPE (99/1)** containing 300 mM sucrose inside and 300 mM glucose outside incubated with **14 µM AH peptide**. Scale bar = 20 µM.

Movie S6. A typical example (2 of 2) of time-lapse sequence of fluorescence images, acquired using spinning disk confocal fluorescence microscopy, of electroformed GUVs consisting of **POPC/Rhodamine-B DOPE (99/1)** containing 300 mM sucrose inside and 300 mM glucose outside incubated with **14 µM AH peptide**. Scale bar = 20 µM.

Movie S7. A time-lapse sequence of fluorescence images, acquired using spinning disk confocal fluorescence microscopy, of electroformed GUVs consisting of **POPC/Rhodamine-B DOPE (99/1)** encapsulating 300 mM sucrose inside and 300 mM glucose outside incubated **with 25 µM 5-TAMRA-AH** peptide. Scale bar = 20 µM.

Movie S8. A time-lapse sequence of fluorescence images, acquired using spinning disk confocal fluorescence microscopy, of electroformed GUVs consisting of

POPC/Rhodamine-B DOPE (99/1) containing 300 mM sucrose inside and 300 mM glucose outside incubated with **35 µM 5-TAMRA-AH** peptide. Scale bar = 20 µM.

Movie S9. A time-lapse sequence of fluorescence images, acquired using spinning disk confocal fluorescence microscopy, of electroformed GUVs consisting of **POPC/Sphingomyelin/Cholesterol/Rhodamine-B DOPE (33/33/33/1)** containing 300 mM sucrose inside and 300 mM glucose outside incubated with **4 µM AH peptide**. Vesicle exterior contains 40 µM **2-NBD-derivatized glucose** (2-NBDG) to monitor any membrane leakage. Scale bar = 30 µM.

Movie S10. A time-lapse sequence of fluorescence images, acquired using spinning disk confocal fluorescence microscopy, of electroformed GUVs consisting of **POPC/Rhodamine-B DOPE (99/1)** with 300 mM sucrose inside and 300 mM glucose outside incubated with **10 µM AH peptide**. Vesicle exterior contains 28 µM **NBDderivatized glucose** (2-NBDG) to monitor any membrane leakage. Scale bar = 30 µM.

Movie S11. Competition assay between electroformed GUVs consisting of **POPC/NBD-PE (99/1)** with 300 mM sucrose inside and 100 nm extruded SUVs consisting of **POPC/Rhodamine-B DOPE (99/1)** with 300 mM sucrose inside monitored using a time-lapse sequence of fluorescence images, acquired using spinning disk confocal fluorescence microscopy. This is a control experiment in which **no AH peptide**

is introduced. Both GUVs and SUVs were osmotically balanced outside with 300 mM glucose. Scale bar = 30 µM.

Movie S12. A time-lapse sequence of fluorescence images, acquired using spinning disk confocal fluorescence microscopy, of a competition assay between electroformed GUVs consisting of **POPC/NBD-PE (99/1)** with 300 mM sucrose inside and 100 nm extruded SUVs consisting of **POPC/Rhodamine-B DOPE (99/1)** with 300 mM sucrose inside. Prior to incubation with **15 µM AH peptide**, GUVs and SUVs were osmotically balanced outside with 300 mM glucose. Scale bar = 30 µM.

Movie S13. A time-lapse sequence of fluorescence images, acquired using spinning disk confocal fluorescence microscopy, of a competition assay between electroformed GUVs consisting of **POPC/NBD-PE (99/1)** with 300 mM sucrose inside and 100 nm extruded SUVs consisting of **POPC/Rhodamine-B DOPE (99/1)** with 300 mM sucrose inside. Prior to incubation with **500 nM AH peptide**, GUVs and SUVs were osmotically balanced outside with 300 mM glucose. Scale bar = 30 µM.

Movie S14 A time-lapse sequence of fluorescence images, acquired using spinning disk confocal fluorescence microscopy, of a fluorescence recovery after photobleaching (FRAP) experiment of an electroformed GUV consisting of **POPC/NBD-PE (98/2)** with 300 mM sucrose inside and 300 mM glucose outside. This is a control for Movies S15S17 **with no AH peptide and no SUVs added**. Scale bar = 30 µM.

Movie S15. Fluorescence recovery after photobleaching (FRAP) of electroformed GUVs consisting of POPC/NBD-PE (98/2) with 300 mM sucrose inside and 300 mM glucose outside. This is a control for Movies S16 & S17 with **POPC/Rhodamine-B DOPE (991)** 100 nm extruded SUVs in 300 mM sucrose added but with **no AH peptide**. Scale bar = 30 µM.

Movie S16. Fluorescence recovery after photobleaching (FRAP) of electroformed GUVs consisting of **POPC/NBD-PE (98/2)** with 300 mM sucrose inside. The GUV exterior contains 100 nm extruded SUVs consisting of **POPC/Rhodamine-B DOPE (99/1)** with 300 mM sucrose inside. Prior to incubation with **2 µM AH peptide**, GUVs and SUVs are osmotically balanced outside with 300 mM glucose. (**NBD CHANNEL**) Scale bar = 30 µM.

Movie S17. Fluorescence recovery after photobleaching (FRAP) of electroformed GUVs consisting of **POPC/NBD-PE (98/2)** with 300 mM sucrose inside. The GUV exterior contains 100 nm extruded SUVs consisting of **POPC/Rhodamine-B DOPE (99/1)** with 300 mM sucrose inside. Prior to incubation with **2 µM AH peptide**, GUVs and SUVs are osmotically balanced outside with 300 mM glucose. (**RHODAMINE CHANNEL**) Scale bar = 30 µM.